Physical properties variations in a shaly formation across a fault core

Audrey Bonnelye, Christian David, Jérôme Wassermann, Alexandre Schubnel, Pierre Henry, Yves Guglielmi, Claude Gout, Pierre Dick

Geophysical Journal International

Geophys. J. Int. (2024) **237,** 1526–1535
Advance Access publication 2024 March 5
GJI Rock and Mineral Physics, Rheology

https://doi.org/10.1093/gji/ggae078

Physical properties variations in a shaly formation across a fault core

Audrey Bonnelye [1,2,3], Christian David [1], Jérôme Wassermann,[4] Alexandre Schubnel,[3] Pierre Henry,[5] Yves Guglielmi,[5] Claude Gout[6,7] and Pierre Dick[8]

[1] *Laboratoire Géosciences et Environnement Cergy, CY Cergy Paris Université, GEC,* F-95000 *Cergy, France. E-mail: audrey.bonnelye@univ-lorraine.fr*
[2] *GeoRessources, Université de Lorraine,* 54000 *Nancy, France*
[3] *Laboratoire de Géologie, Ecole Normale Supérieure,* 75005 *Paris, France*
[4] *Laboratoire de Mécanique et Matériaux du Génie Civil, CY Cergy Paris Université,* F-95000 *Cergy, France*
[5] *CNRS, IRD, INRAE, Coll France, CEREGE, Aix Marseille Univ, Aix-en-Provence, France*
[6] *LFCR, UPPA, CNRS, Pau, France*
[7] *Université de Pau et des Pays de l'Adour, E2S UPPA, CNRS, TotalEnergies, LFCR, Pau, France*
[8] *PSE-ENV/SEDRE/LETIS, Institut de Radioprotection et de Sûreté Nucléaire (IRSN),* 92260 Fontenay-aux-Roses*, France*

Accepted 2024 February 12. Received 2024 January 17; in original form 2022 April 1

SUMMARY

Faults in general, and in clay materials in particular, have complex structures that can be linked to both a polyphased tectonic history and to the anisotropic nature of the intact rock. Drilling through faults in shaly materials allows measuring properties such as the structure, mineralogical composition, stress orientation and physical properties. We combine different petrophysical measurements on core samples retrieved from a borehole drilled perpendicularly to a fault zone affecting Toarcian shales from the Tournemire underground research laboratory (France). The borehole is cross-cutting the entire fault thickness which is of the order of 10 m. We perform several types of measurements: density, porosity, saturation directly in the field and *P*-wave velocities together with *P*-waves anisotropy on core samples taken at regular intervals. Special protocols were developed to preserve as much as possible the saturation state of the samples. From our measurements, we were able to track the increase of damage, characterized by a smooth decrease in elastic moduli from the intact zone to the fault core. We then calculated Thomsen's parameters to quantify the elastic anisotropy evolution across the fault. Our results show strong variations of the elastic anisotropy with the distance to the fault core as well as the occurrence of anisotropy reversal.

Key words: Fault zone rheology; Geomechanics; Seismic anisotropy.

1 INTRODUCTION

Faults in general, are characterized by two distinct zones as follows (Caine *et al.* 1996; Ben-Zion & Sammis 2003; Faulkner *et al.* 2010): a more or less narrow (e.g. <10 cm San Gabriel Fault in San Andreas system, Chester *et al*. 1993) Fault Core (FC) with localized deformation and relatively low permeability, and a Fault Damage Zone (FDZ) bounding the fault core which accommodates strain and displacement variations (Peacock *et al*. 2017). The fault zone thickness can reach several tens of meters in length, depending on the tectonic history and displacement along the fault plane, the nature of the host rock imbedding the fault will in turn infer on its mechanical properties and anisotropy (Faulkner *et al.* 2008, 2011; Rempe *et al.* 2013). One of the main difficulties in describing these structures is to find a clear definition for each zone. When referring to the FDZ, one key parameter to describe it is the fracture density. This parameter can be evaluated via different methods such as outcrop analysis, drilling data analysis and seismic data interpretation (Mitchell & Faulkner 2012; Choi *et al.* 2016; Gomila *et al.* 2016; Torabi *et al.* 2020). This approach allows for a better understanding of the fault as the fracture density calculation will enable to make assumption both on the evolution of the stiffness and the fluid circulation across the fault. However, when looking closely at the microstructures of samples coming from major drillings [San Andreas Fault Observatory at Depth—SAFOD (Solum *et al.* 2006; Janssen *et al.* 2012), Japan Trench Fast Drilling Project—JFAST (Yamaguchi *et al.* 2011) or Taiwan Chelungpu-Fault Drilling Project—TCDP (Hirono *et al.* 2014)], we can observe that in addition to the fractures, there is a complex organization of the minerals—such as mineral re-orientation—that is not necessarily the expression of these fragile deformation mechanisms. These studies report the presence of clay minerals in fault cores, that can

strongly affect the behaviour of faults by reducing friction (Saffer & Marone 2003; Ikari *et al.* 2007; Collettini *et al.* 2009), permeability (Mitchell & Faulkner 2012; Dick *et al.* 2016) and elastic properties. Nevertheless, due to the high cost of such projects and technical difficulties, it is very hard to get very detailed description of the whole faults.

On the other hand, Underground Research Laboratories (URL) give the opportunity to have an easier access to smaller features that can give insights on faults structures. Due to conditions of drilling in URL (shallow depth, shorter boreholes, easy access to fault zones), the sample recovery can be up to 100 per cent of the borehole. In addition, such studies represent unique chances to perform multidisciplinary studies on fault zones, and providing laboratory petrophysical measurements on core samples allows for comparison with geophysical studies performed in the zone. In our case, we can study in detail a fault zone, located in a shale layer, thanks to a fully cored borehole. Measurements of rock physical properties at the laboratory scale help quantifying fault material fabric structural variations that can be linked to fault macrostructures and to the overall faulting mechanisms. For instance, rock physical properties (especially elastic properties) can be a proxy for quantifying the damage that rocks may have experienced due to tectonic forces (Jones & Wang 1981; Vernik & Nur 1992; Cholach & Schmitt 2006; Moreno *et al.* 2018) or stress variations due to excavation (Blümling *et al.* 2007). Such damage characterization can be done through acoustic elastic wave velocity measurements (Josh *et al.* 2012). However, measuring the *P*-wave velocities in shaly materials is difficult, first because clay rich rock properties are highly sensitive to temperature and relative humidity (Hedan *et al.* 2012). Secondly, clay rocks often display a high anisotropy due to a superposition of different causes (sedimentary nature, shape of clay minerals, shape of pore network), that needs to be considered in the measurement protocol. In this context, one approach is to integrate several complementary measurement types such as *P*-wave velocity, permeability or anisotropy of magnetic susceptibility (Schubnel & Guéguen 2003; Schubnel *et al.* 2006; David *et al.* 2007; Josh *et al.* 2012; Faoro *et al.* 2013; Bonnelye *et al.* 2017a; Geng *et al.* 2017, 2018).

Given that fault zones geometry and physical properties is of paramount relevance in order to unravel their complex behaviour, we propose here to link the tectonic description with physical parameters. In this paper, we present a combination of density, saturation and *P*-wave velocity anisotropy measurements performed on shale samples retrieved from a borehole drilled across a fault zone affecting a clay formation. This study is part of a larger project that included a fluid injection experiment meant to hydromechanically reactivate a small scale strike-slip fault outcropping at the Tournemire URL in order to explore the relationships between fault movements, leakage and induced seismicity (Guglielmi *et al.* 2015; De Barros *et al.* 2016). All along the borehole, density and porosity were measured onsite in the URL (14 °C, RH = 90 per cent), on core samples retrieved immediately after drilling. Additional samples were conditioned for *P*-wave velocity measurements at the rock physics laboratory of CY Cergy Paris University. These measurements include 90 velocity measurements per sample in order to capture the whole anisotropy of the clay material. We observe rock physics signatures specific to the host rock, the fault damage zone (FDZ) and the fault core zone (FCZ). Our measurements, combined with microstructural observations, allow us to discuss the active mechanisms involved in fault rupture localization.

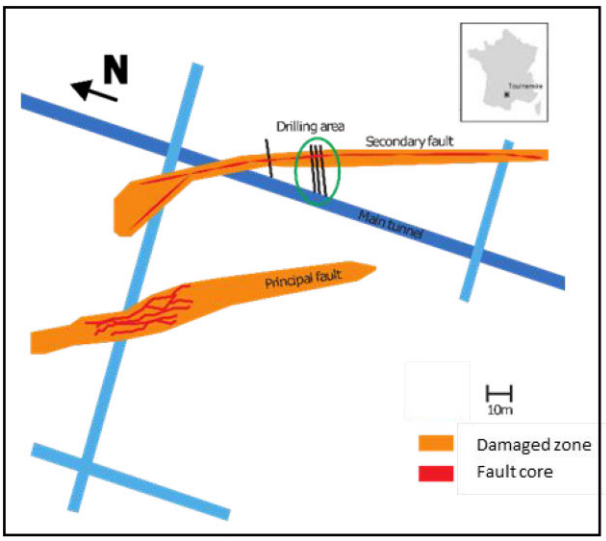

Figure 1. Map of the Tournemire underground research laboratory and localization of the secondary fault zone studied, with the Fault Damage Zone (FDZ) in orange and the Fault Core Zone (FCZ) in red. The structure of the fault was determined by structural mapping along the galleries (the main tunnel is in dark blue and the galleries are in light blue) and from more than 30 boreholes that have cross cut the fault zones.

2 AREA OF INTEREST AND STUDIED MATERIAL

2.1 Area of interest

The underground research laboratory (URL) at Tournemire, France is managed by the French national public expert in nuclear and radiological risks (IRSN). The URL was excavated from a 135-yr-old railway tunnel and is devoted to research programs concerning the disposal of radioactive waste in a clay-rich rock formation. For this purpose, six galleries were excavated between 1996 and 2008 in a 200-m-thick subhorizontal layer of Toarcian shale. The URL is located on the Western border of the Mesozoic sedimentary Causses Basin (SW France) that has undergone two main tectonic regimes:

(i) A north–south extension during the Upper Jurassic associated to the period of maximum burial for the Toarcian layer (at least 2.2 km corresponding to about 60 MPa burial stress (Séranne 2014) under a deviatoric tectonic stress of about 80 MPa (Constantin *et al.* 2004).

(ii) A NE/SW to NW/SE compression during the mid-Cretaceous Pyrenean orogeny. The burial stress decreased as well as the maximum deviatoric stress estimated to 40–50 MPa (Constantin *et al.* 2007).

The fault studied in this work is the so-called 'secondary fault' in Fig. 1(a). It is a reverse left-lateral strike-slip fault with a N170°-to-N010° dip direction and 60°-to-80°W dip (for structural details see Lefèvre *et al.* 2016). Schematically, the actual fault structure results from the combination of the two major tectonic periods described above.

2.2 Studied material

The Tournemire host rock has been extensively studied. It is a shale with a natural water content varying from 3.5 to 8 per cent (Masri *et al.* 2014), an average bulk density of 2.57 (±0.06) g cm^{-3}, and

a porosity ranging from 6.5 to 7.1 per cent. The average composition of this shale is 15–25 per cent illite, 15–25 per cent smectite and kaolinite, 10–30 per cent calcite and dolomite, 10–20 per cent quartz. Detailed information on the Tournemire URL and on the petrophysical properties of the shale are provided in Cabrera *et al.* (2001), Valès *et al.* (2004) and Geng *et al.* (2017). The anisotropy of mechanical properties has also been thoroughly investigated (Niandou *et al.* 1997; Bonnelye *et al.* 2017a), as well as the acoustic response during deformation (Bonnelye *et al.* 2017b). Our samples come from borehole HS1 (Fig. 2), which has been air-drilled to a total length of 21 m to limit the perturbations to the saturation state and the fluid chemistry inside the material. The 50 mm diameter cores were recovered in metre-long core liners to preserve as much as possible the damaged and fault core zones structures (we had a recovery rate of almost 100 per cent). Core samples of 15 cm length were collected every metre along the borehole and were vacuum packed in aluminium bags in order to preserve their initial water content for later elastic wave velocity measurements in the laboratory. Core density and porosity were measured directly in the URL within hours after retrieval from the drilling borehole.

3 METHODS

3.1 On-site measurements

During the drilling operations, a precise visual description of the recovered cores has been done, allowing for structural description but also orientation of all samples. Measurements of density and porosity were performed in the tunnel where samples were broken into pieces to use only the central part of the core, thus avoiding drilling-induced desiccation/desaturation. Measurements were made on a set of three small samples every 50 cm to ensure measurement repeatability. We adopted the triple weight method described in Matray *et al.* (2007) to determine the bulk density, water content and porosity using a dearomatized petroleum solvent. These on-site measurements were used to determine porosity and saturation. Helium pycnometry measurements were performed later at IRSN on the same samples. The porosity ϕ estimated with this method corresponds to the connected or open porosity where Helium flow can penetrate the sample. Porosity is calculated with eq. (1):

$$\phi = \frac{V_{\text{pores}}}{V_{\text{tot}}} = 1 - \frac{M_t}{\rho_s V_{\text{tot}}}, \quad (1)$$

where M_t is the mass of the sample dried at temperature t (105 °C), and ρ_s the grain density measured by helium pycnometry. The total volume V_{tot} is estimated in the field from the oil volume displaced when immersing the sample into the oil tank.

3.2 Elastic wave velocity measurements

A new experimental setup adapted from the one described in David *et al.* (2017) was developed at CY Cergy Paris University. This device measures the *P*-waves traveltimes across several diameters in cylindrical samples (diameter 53 mm) and under controlled relative humidity in a closed chamber. The sample is rotated with 1.8° angular increments (Figs 2b and c) to characterize the angular variations of the *P*-wave velocity. In order to achieve representative measurements, dedicated samples were selected in which no apparent heterogeneities (such as fractures or fossils) could be visually identified at the sample surface.

The device is water vapour controlled, and the relative humidity in the chamber is maintained between 90 and 100 per cent thanks to saturated salt solutions of potassium sulfate. A measurement cycle begins first by tightly applying both ultrasonic *P*-wave transducers across the diameter of the sample by means of two linear actuators. The contact force applied to the transducers is controlled by a piezo-resistive force sensor for repeated measurements. Force is held constant during all the measurement cycle. Because of the relative weakness of the studied material, the applied force is kept low to avoid breaking the sample during the measurements as the tensile strength is low. The ultrasonic sensors have a 0.5 MHz central frequency. The coupling between the sensors and the sample is achieved through rubber buffers and a coupling gel. A Panametrics 5058PR pulse generator sends a 400 V amplitude pulse to the transmitter and the waveform caught by the receiver is recorded with a sampling frequency of 10 MHz. The recording of the signal is triggered by the first pulse sent to the emitter and lasts 1×10^{-3} s. After one measurement cycle, the ultrasonic sensors are removed from the sample which is rotated by an angle of 1.8°. A new measurement cycle is then conducted with this new sample orientation. An Arduino microcontroller and a computer for data acquisition and processing control each operation. Each cycle generates several waveforms recorded by the receiving sensor and stored on the computer to be used later for estimating the time of flight of the *P* wave. These waveforms are stacked to increase the signal to noise ratio. The *P*-wave traveltime is automatically detected from the stacked signal using the Akaike Information Criterion (AIC) method (Akaike 1974; Zhang 2003); David *et al.* 2017).

4 RESULTS

4.1 On-site observations and measurements

In the intact zone of the Western fault compartment, from 1.5 to 12.5 m depth, the core samples seem to be homogeneous with sometimes some fossils (Fig. 3b). It is possible to clearly identify the bedding planes. A few small fractures could be observed that are mostly located in the shallow borehole segment corresponding to the Excavation Damage Zone (EDZ which extends about 2 m away from the tunnel wall). The porosity values show a slight increase from 10 to 12 per cent with an inflection point located 2 m before the identified FDZ. Similarly, dry density variations show symmetrical opposite variations from 2.4 to 2.35. In the Eastern fault compartment, the intact rock is observed from 19 to 21 m depths. The porosity is slightly lower and the density slightly higher than in the intact Western compartment. This difference may be related to the offset of the fault which is ∼5 m; the observed borehole is sampling different stratigraphic layers from the Eastern and Western compartments, with slightly different porosity and density

The FDZ is identified during core inspection by the presence of both calcified and non-calcified fractures (Fig. 3c). Between these structures, the rock looks intact, with sub-horizontal bedding plane. Note that fractures have various orientations. This area stretches from 12.5 to 15 m in the Western compartment and from 17.5 to 19 m in the Eastern compartment. In the FDZ, porosity increases from ∼12 to ∼15 per cent close to the fault core. The dry density varies in the range of 2.35–2.30 g cm^{-3}.

The FC contains both calcified fractures and non-calcified fractures. Compared to FDZ, fractures display slickensides and a thin

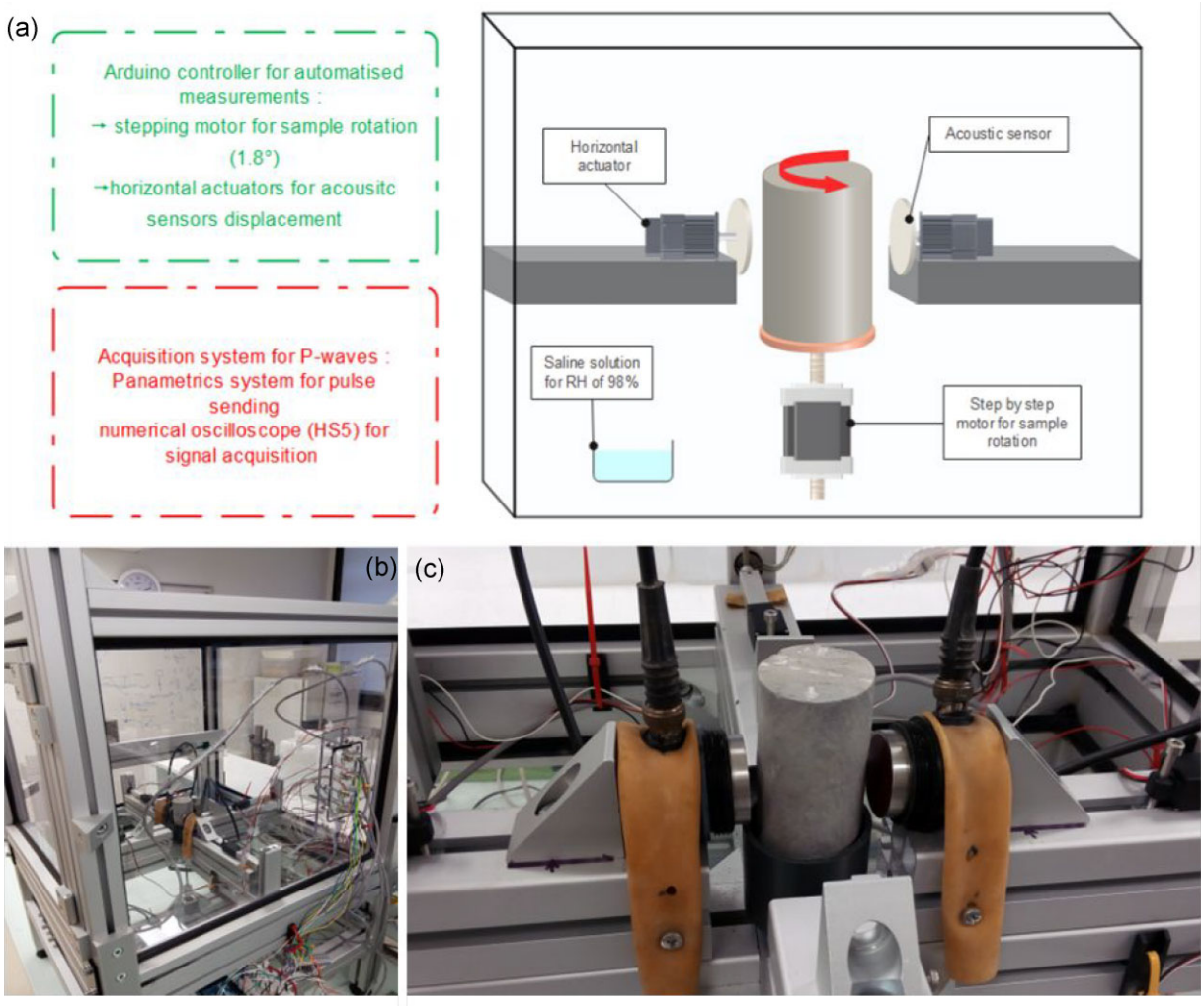

Figure 2. (a) Scheme of the experimental setup used for the measurement, (b) humidity-controlled air-tight chamber used for the fully automated elastic wave velocity measurements. (c) Close-up on the sample located between two ultrasonic transducers.

layer of black gouge with no clear foliation (Fig. 3d). In most parts of the fault core, the original orientation of the bedding is not visible, but it is possible to observe schistosity parallel to the fault. In some sections where the cores appear homogeneous, the bedding planes are observed, crosscut by veins or fractures. Both the largest (∼15 per cent) and lowest (∼3 per cent) porosities were measured in the fault core, corresponding respectively to the lowest (∼2.2 g cm^{-3}) and largest (∼2.6 g cm^{-3}) dry density.

The fault has an asymmetric structure with an FDZ thicker in the Western compartment (∼5 m) than in the Eastern compartment (∼1 m). Porosity and density variations correlate spatially with fault structure. Moreover, our systematic multiple measurements, as shown by our low standard deviations values (Table 1), allow us to be confident enough to conclude that the data scatter in the fault core is due to the strong heterogeneity of this zone.

4.2 Elastic wave velocities

As the borehole was drilled in a subhorizontal direction (15° dip) parallel to the bedding's strike, and because the bedding in the Tournemire argillite is also subhorizontal (12° dip), *P*-wave anisotropy is easily observed from the radial measurements following our methodology. The *P*-wave velocity measurements are presented in Fig. 4(a) as a function of both the angle θ relatively to the bedding plane, with the convention that $\theta = 0°$ corresponds to the normal to the bedding plane in agreement with Thomsen's convention (Thomsen 1986), and as a function of the distance to the borehole mouth.

The recorded signals display a low signal-to-noise ratio (SNR) due to high attenuation along the ray path. For this reason, the automatic detection of *P*-wave velocities near 0° remains difficult in all the samples. Thus, we decided to discard the values between 0° and 15° that are not shown in Fig. 4(a). Nevertheless, some outliers remain in Fig. 4(a) related to automatic detection errors given the low SNR.

In the intact zone, the *P*-wave velocity anisotropy of the three samples in the first 5 m is almost the same: the minimum velocity is measured perpendicular to the bedding and is around 2400 m s^{-1}, and the maximum velocity of about 3400 m s^{-1} is measured parallel to the bedding. Thereafter, a downward shift of the sinusoid reflecting a slight decrease in velocity of about 100 m s^{-1} is observed when approaching the damaged zone (Fig. 4a, green surface). Finally, the velocities in the intact Eastern compartment are higher

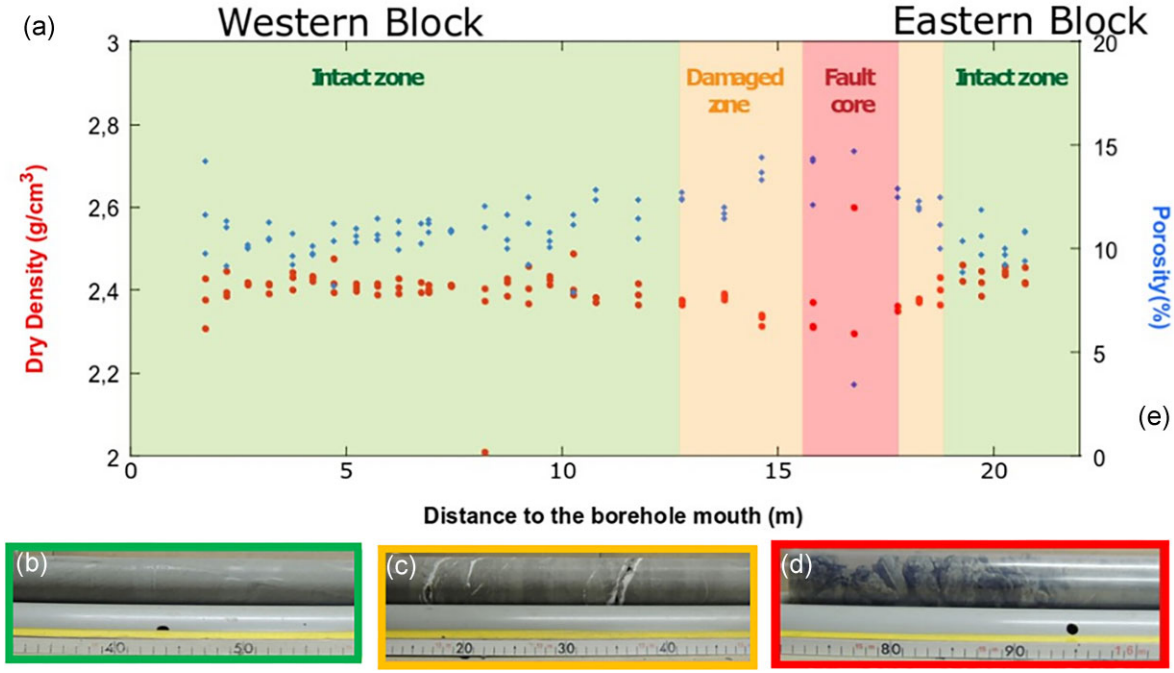

Figure 3. (a) Dry density (red dots) and porosity (blue diamonds) with respect to the distance to the borehole mouth in the main tunnel (see Fig. 1b for borehole location). The background colours correspond to the different zones identified from on-site qualitative observations on the core samples retrieved from the borehole. (b, c, d) Pictures of recovered material from the intact zone, damaged zone, fault core (with core liner for better recovery), respectively.

Table 1. Average dry density and porosity with standard deviations in the different zones (IZ = Intact Zone, DZ = Damaged Zone, FC = Fault Core, E = Eastern compartment, W = Western compartment).

	IZ-W	DZ-W	FC	DZ-E	IZ-E
Dry density (g cm^{-3})	2.8	2.8	2.7	2.7	2.7
standard deviation	0.2	0.2	0.1	0.1	0.1
Porosity (per cent)	11.0	12.0	13.9	11.9	10.2
standard deviation	2.3	1.4	1	0.9	0.8

than in the Western compartment, respectively of 2800–3600 and 2400–3600 m s^{-1}.

In the FDZ of the Western block, the velocities decrease slightly to 2200 and 3200 m s^{-1} and the anisotropy is smaller. A comparison of the velocity measurements on a sample coming from the intact zone and the FDZ clearly shows the differences in values in Fig. 4(b). In the fault core, the material is fragmented and highly attenuating, so that the *P*-wave arrival times were undetectable automatically. Velocities were measured manually and in two directions only, parallel and perpendicular to the oriented recovered material. The manual velocity measurements (Fig. 4c) exhibit a slight difference of values compared to automatic ones because the pressure applied to perform the measurements is higher during the manual measurements than during the automatic ones. These velocity measurements show values below 1500 m s^{-1} and a weak-to-no anisotropy, between 16 and 17 m depths (i.e. in what was identified as the FC). This very low velocity can be explained by the friability of the sample and its high porosity.

Finally, Thomsen's parameters (Thomsen 1986) ε and α are estimated with available data along the borehole (Fig. 4d). Parameter ε quantifies the *P*-wave anisotropy ($\varepsilon = [V_P(90^\circ) - V_P(0^\circ)]/V_P(0^\circ)$)and parameter α is the *P*-wave velocity propagating perpendicular to the bedding ($\alpha = V_P(0^\circ)$). This allows to quantify the drop in anisotropy that was observed in the dataset as ε decreases from 0.4 to 0.2 in the FDZ and drops close to 0 (i.e. no or close to no anisotropy) in the FC.

5 DISCUSSION

Seismic anisotropy studies are a common tool in the frame of large scale investigation of regional faults studies (Crampin & Peacock 2005). The variations are used to highlight preferred orientations of minerals, or cracks parallel to the fault as indicators of stress concentration in the vicinity of the fault (Huang *et al.* 2019; Arai *et al.* 2020; Wang *et al.* 2020). In the present case, a variation of anisotropy is clearly identified from the host rock towards the fault core. The intact rock is already anisotropic due to the sedimentary nature of the rock. This can be observed in our measurements, in Fig. 4(a), in the part highlighted in green, corresponding to the intact zone where the velocity varies between 3500 and 2500 m s^{-1}. When moving towards the damaged zone and fault core, the *P*-wave velocities are decreasing in general, as well as the anisotropy. The evolution of the anisotropy highlighted here can be the result of the superposition of different effects: bedding rotation and microfractures linked to the shear zone. These fractures can be free or filled with calcite. These factors will influence the evolution of the velocities and so of the anisotropy. It is observed that Thomsen's parameter ε is changing from 0.4 to 0.2 in the damaged zone and close to 0 in what we identified as the fault core. Our data set is following the common trend observed at large scale with low spatial resolution from data logging performed on scientific drillings; indeed, a decrease of velocities (Jaeggi *et al.* 2017) and increase in porosity were observed in the vicinity of the fault zone (Hung *et al.* 2009; Conin *et al.* 2011; Savage *et al.* 2021). Porosity evolution can also exhibit a complex evolution when observed at the scale of the borehole in URL, for example the main fault at Mont Terri (Orellana *et al.* 2022) and in that case, it is shown that within the fault core the porosity can either increase or decrease compared to

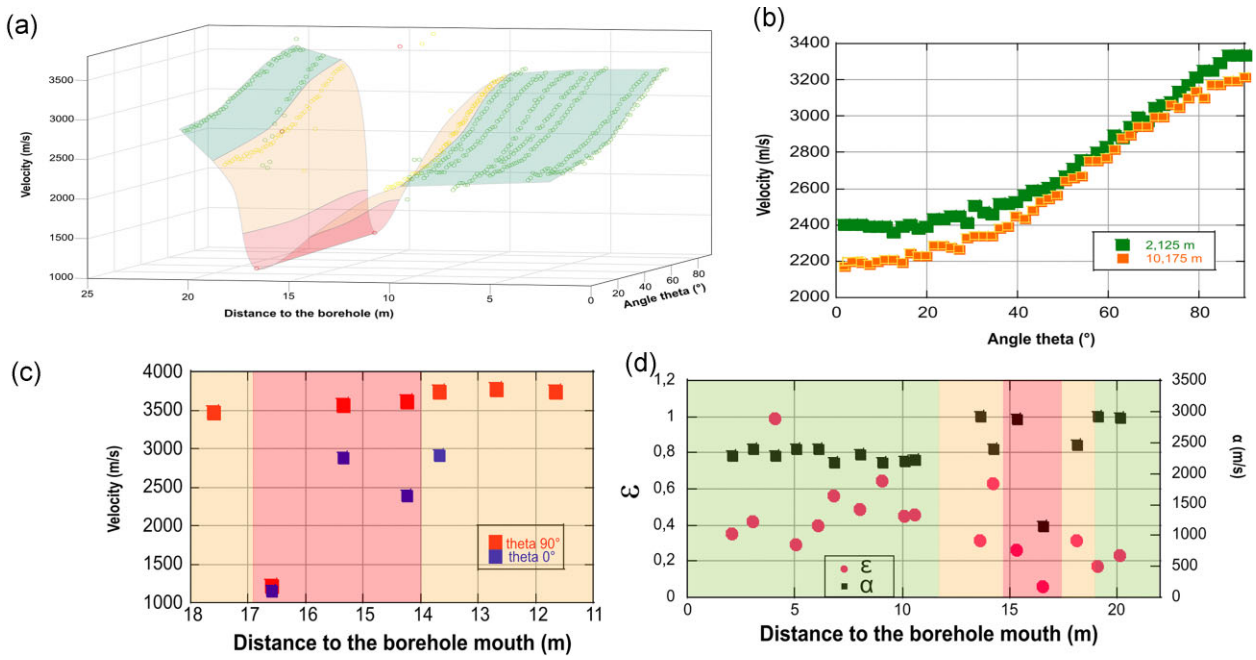

Figure 4. (a) *P*-wave velocities (m s^{-1}) as a function (i) of the angle θ measured with respect to the normal to the bedding plane and (ii) of the distance to the borehole mouth (m). The surfaces denote the trend, the colours figure the zones, respectively green for the intact rock, yellow for the FDZ and red for the fault core. (b) Examples of velocities measured around samples taken from the intact zone (green) and FDZ (yellow). (c) Manual measurements of velocities parallel (red) and perpendicular (blue) to the bedding conducted in the FDZ and FC (i.e. between 11 and 18 m from the borehole mouth). (d) Thomsen's parameters ε and α estimated with respect to the distance to the borehole mouth.

the intact rock, depending whether it is the gouge or the scaly clay that is measured. An increase of porosity can actually explain the global trend of decreasing velocity in our case, but not the variation of anisotropy. Microstructural observations performed in similar conditions and focusing on fault structure are supporting our observations linked to a potential mineral re-orientation affecting the anisotropy (Laurich *et al.* 2014; Jaeggi *et al*. 2017; Laurich *et al.* 2017). At large scale it is usually the bedding orientation taken from log that are indicating the fault (Cook *et al.* 2020). The fault studied here is composed of a relatively wide FC (∼1 m) compared to some observations made on active faults where the slip zone in major faults can be thinner, only a few cm. This zone is surrounded by a FDZ where our measurements show velocities perturbations despite the fact that the selected samples were selected without apparent macroscopic failure. In the far field, the intact rock displays relatively homogenous anisotropic velocity properties. The transition between these zones is very smooth and our observations and measurements suggest the existence of a continuum of deformation rather than sharp boundaries (Fig. 5).

Some samples were observed under SEM (scanning electron microscope). They were all recovered in the FDZ and in the FC. In the FDZ (Figs 6a and d), a relatively undeformed material with only a small shearing plane with slickensides is observed. In the FC, two facies were observed: some exhibiting scaly facies and kinked minerals (Fig. 6b) and some exhibiting dark gouge with strong slickensides marks, similar to what is observed also in other faults in similar rock types like in the Mont Terri URL (Laurich *et al.* 2014).

These microstructures highlight the numerous different microfacies that can be found inside and near the FCZ. Both the fractures and disorientation of clay aggregates can explain the decrease in velocity and anisotropy in the FDZ and in the FC. These results are in good agreement with our previous studies. A decrease and a reversal of anisotropy were measured in the laboratory during triaxial tests on the Tournemire shale when approaching the shear failure stress as well as after shear localization (Geng *et al.* 2017). These observations were explained by crack propagation and mineral re-orientation, the later acting as a mechanism allowing for final fracture localization. The 40 MPa of confining pressure required in the laboratory to make such observations is equivalent to the one estimated during the extension phase undergone by the Tournemire shales during the Upper Jurassic. As the diffuse deformation, for example rotated lenses, seems to be overprinted by the small fracture, it is probably an early mechanism enabling the localization of deformation. This pre-deformed state can be seen as a mechanical weakness in which the deformation localization would be easier during the second tectonic phase related to the Pyrenean compression, during which more non-continuous localized deformation can occur such as slipping and formation of black gouge.

From a methodological viewpoint, the fully automated (from the precise positioning of the ultrasonic sensors to the waveform recording and traveltime picking) radial *P*-wave measurements with a fine angular step performed in this study allows detecting and analysing anisotropy variations with a high accuracy. Here the *P*-wave velocity variations are much stronger than what can be observed via conventional imaging methods on larger scales (Esefelder *et al.* 2021) because the measured anisotropy depends strongly on the wavelength and the resolution of the method, and so of the scale of the origin of the anisotropy. In the same URL at Tournemire, some *in situ* seismic measurements were performed recently, both in a passive and active mode. These studies were conducted with seismic sensors with a much lower frequency than ours, under the actual *in situ* conditions σ_1 and σ_3 between 3 and 5 MPa): the average *P*-wave velocity found was higher than our values, around 3500 m s^{-1} (Bretaudeau *et al.* 2014; Nhu 2014; Rivet *et al.* 2016). The anisotropy estimated in these studies at the field scale was lower

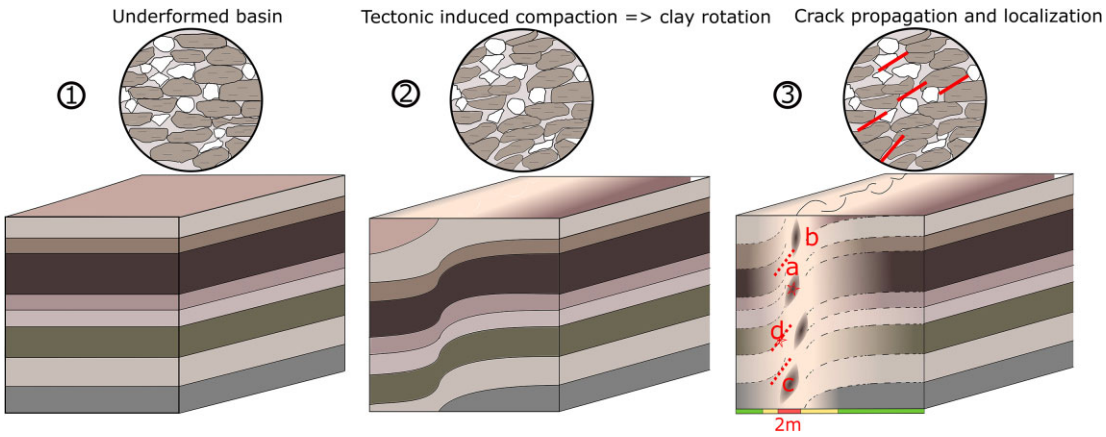

Figure 5. Schematic view of a fault in shales with microstructures taken in a borehole drilled through the same fault. The variation of bedding orientation during fault formation is a possible explanation for the rotation of anisotropy.

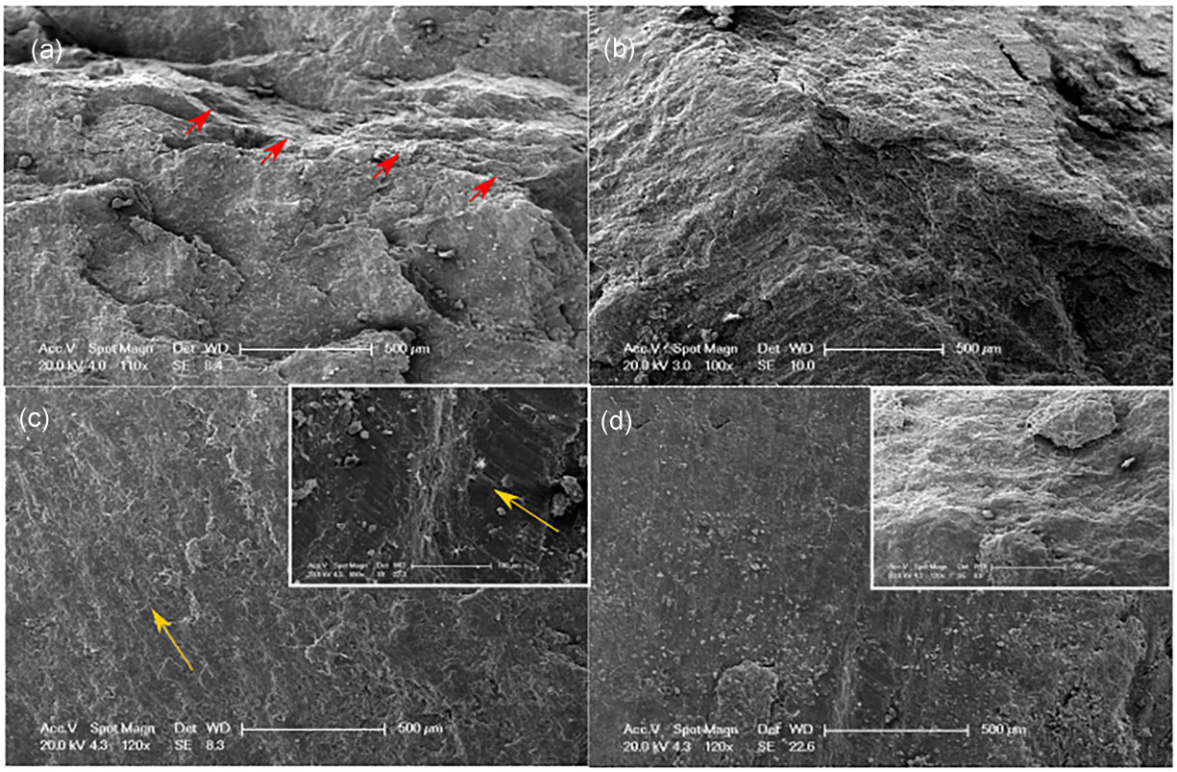

Figure 6. SEM images of samples taken along the borehole. The locations are denoted in Fig. 5. (a) Sample taken in the fault core (17.84–17.86 m) exhibits anastomosed spaced formation (scaly fabric, underlined by red arrows) with kinked minerals and shearing planes. (b) Fault core (16.62–16.63) with slight slip marks. (c) Gouge zone (17.86–17.87) in the breccia zone and slip marks (direction of slip showed with yellow arrows). (d) Damaged zone (17.87–17.90 m) exhibiting very few deformation patterns on the Western block.

than ours, around 10 per cent. Again, this can be due to the different measuring conditions (frequency, *in situ* versus ambient conditions, or the fact that anisotropy tends to decrease with increasing confining pressure) but it mostly reflects the crucial question of scaling between laboratory measurements and geophysical observations. Indeed, due to the different frequencies used for geophysical survey and for petrophysical measurements in the laboratory, they are not sensitive to the same size of defect (Bailly *et al.* 2019). Thus, it raises the question of what should be accounted for when looking at the influence of the FDZ on the mechanical properties of the entire fault zone and if the fracture density is sufficient or could be completed by other quantifying methods. Furthermore, the variations observed here have a similar value than what can be observed on large scale faults. Such variations in term of velocity and porosity can have a strong impact on important parameters controlling the mechanical behaviour of fault zones: their elastic properties and so the distribution of stresses on the fault plane, the permeability and so fluid path and fluid overpressures. In our case, we link the mechanisms of fault formation with the fault structure. The rotation of anisotropy (Fig. 5) as well as the formation of scarce slip zone can

potentially generate heterogeneities along the fault core in terms of elastic properties as well as in terms of permeability.

6 CONCLUSION

Small changes in *P*-wave velocities and anisotropy were found in visually intact core samples in the Tournemire fracture damage zone and core zone. A smooth transition from the intact zone to the fault damage zone, then to fault core zone is observed in these visually intact blocks. A drop in *P*-wave velocity in the core zone of the order of 40 per cent is measured with respect to the intact zone.

More importantly, these petrophysical measurements of cores from a natural fault zone that has been extensively studied are providing an interesting example of the important difference between laboratory scale measurement and field scale measurements. The dataset is showing strong disturbance of the anisotropy towards the fault core. This rotation is in good agreement with observations of faults acting like barriers for fluid at the interface between the FC and the DZ. The analysis of the evolution of *P*-wave anisotropy allowed us to propose a model of deformation mechanisms occurring during fault formation. Understanding the architecture of faults, and more importantly, being able to find physical signature of geometry changes is of paramount relevance for a better assessment of fault mechanical behaviour. Nevertheless, the question of accounting for different scales of discontinuities and variation of anisotropy is still essential and it would be crucial to understand it from a geomechanical point of view in order to understand how to account for local heterogeneities in large scale models.

ACKNOWLEDGMENTS

We are thankful to Alain Tonetto from the Fédération de Chimie in Aix-Marseille Université for providing us the SEM images from the fault. This study was performed in the frame of the Fluids and Faults project funded by TotalEnergies.

SUPPORTING INFORMATION

Supplementary data are available at *GJI* online.

Supp-Info

Please note: Oxford University Press is not responsible for the content or functionality of any supporting materials supplied by the authors. Any queries (other than missing material) should be directed to the corresponding author for the paper.

DATA AVAILABILITY

The data underlying this paper will be shared on reasonable request to the corresponding author.

REFERENCES

Akaike, H., 1974. Markovian representation of stochastic processes and its application to the analysis of autoregressive moving average process. *Ann. Inst. Stat. Math.,* **26,** 363–387.

Arai, R., Kodaira, S., Henrys, S., Bangs, N., Obana, K., Fujie, G., Miura, S. *et al.*, 2020. Three-dimensional *P* wave velocity structure of the Northern Hikurangi margin from the NZ3D experiment: evidence for fault-bound anisotropy. *J. geophys. Res.,* **125**(12), doi:10.1029/2020JB020433.

Bailly, C., Fortin, J., Adelinet, M. & Hamon, Y., 2019. Upscaling of elastic properties in carbonates: a modeling approach based on a multiscale geophysical data set. *J. geophys. Res.,* **124**(12), 13 021–13 038.

Ben-Zion, Y. & Sammis, C.G., 2003. Characterization of fault zones. *Pure appl. Geophys.,* **160,** 39.

Blümling, P., Bernier, F., Lebon, P. & Martin, C.D., 2007. The excavation damaged zone in clay formations time-dependent behaviour and influence on performance assessment. *Phys. Chem. Earth, Parts A/B/C,* **32**(8–14), 588–599.

Bonnelye, A., Schubnel, A., David, C., Henry, P., Guglielmi, Y., Gout, C., Fauchille, A.-L. & Dick, P., 2017a. Elastic wave velocity evolution of shales deformed under uppermost crustal conditions: elastic anisotropy of shales. *J. geophys. Res.,* **122**(1), 130–141.

Bonnelye, A., Schubnel, A., David, C., Henry, P., Guglielmi, Y., Gout, C., Fauchille, A.-L. & Dick, P., 2017b. Strength anisotropy of shales deformed under uppermost crustal conditions: strength anisotropy of shales. *J. geophys. Res.,* **122**(1), 110–129.

Bretaudeau, F., Gélis, C., Leparoux, D., Brossier, R., Cabrera, J. & Côte, P., 2014. High-resolution quantitative seismic imaging of a strike-slip fault with small vertical offset in clay rocks from underground galleries: experimental platform of Tournemire, France. *Geophysics,* **79**(1), B1–18.

Cabrera, J. *et al.*, 2001. Projet Tournemire–Synthèse Des Programmes de Recherche 1995-1999, Rapport IRSN: DPRE/SERGD01–19.

Caine, J.S., Evans, J.P. & Forster, C.B., 1996. Fault zone architecture and permeability structure. *Geology,* **24**(11), 1025–1028.

Chester, F.M., Evans, J.P. & Biegel, R.L., 1993. Internal Structure and Weakening Mechanisms of the San Andreas Fault. *J. geophys. Res.,* **98**(B1), 771–786.

Choi, J.-H., Edwards, P., Ko, K. & Kim, Y.-S., 2016. Definition and classification of fault damage zones: a review and a new methodological approach. *Earth Sci. Rev.,* **152**(January), 70–87.

Cholach, P.Y. & Schmitt, D.R., 2006. Intrinsic elasticity of a textured transversely isotropic muscovite aggregate: comparisons to the seismic anisotropy of schists and shales. *J. geophys. Res.,* **111**(B9), doi:10.1029/2005JB004158.

Collettini, C., Niemeijer, A., Viti, C. & Marone, C., 2009. Fault zone fabric and fault weakness. *Nature,* **462**(7275), 907–910.

Conin, M., Henry, P., Bourlange, S., Raimbourg, H. & Reuschlé, T., 2011. Interpretation of porosity and LWD resistivity from the Nankai accretionary wedge in light of clay physicochemical properties: evidence for erosion and local overpressuring. *Geochem. Geophys. Geosyst.,* **12**(3), doi:10.1029/2010GC003381.

Constantin, J., Laurent, P., Vergély, P. & Cabrera, J., 2007. Paleo-deviatoric stress magnitudes from calcite twins and related structural permeability evolution in minor faults: example from the Toarcian Shale of the French Causses Basin, Aveyron, France. *Tectonophysics,* **429**(1–2), 79–97.

Constantin, J., Peyaud, J.B., Vergély, P., Pagel, M. & Cabrera, J., 2004. Evolution of the Structural Fault Permeability in Argillaceous Rocks in a Polyphased Tectonic Context. *Phys. Chem. Earth, Parts A/B/C,* **29**(1), 25–41.

Cook, A.E. *et al.*, 2020. Physical properties and gas hydrate at a Near-Seafloor Thrust Fault, Hikurangi Margin, New Zealand. *Geophys. Res. Lett.,* **47**(16), e2020GL088474.

Crampin, S. & Peacock, S., 2005. A review of shear-wave splitting in the compliant crack-critical anisotropic Earth. *Wave Motion,* **41**(1), 59–77.

David, C., Robion, P. & Louis, L., 2017. A single laboratory setup for investigating the anisotropy of both seismic and electrical properties in core samples. *Geophys. J. Int.,* **210**(3), 1595–1608.

David, C., Robion, P. & Menéndez, B., 2007. Anisotropy of elastic, magnetic and microstructural properties of the Callovo-Oxfordian Argillite. *Phys. Chem. Earth, Parts A/B/C,* **32**(1–7), 145–153.

De Barros, L. *et al.*, 2016. Fault structure, stress, or pressure control of the seismicity in shale? insights from a controlled experiment of fluid-induced fault reactivation: seismicity controlling factors in shale. *J. geophys. Res.,* **121**(6), 4506–4522.

Dick, P. *et al.*, 2016. The internal architecture and permeability structures of faults in shale formations, in *The Clay Minerals Society Workshop Lectures Series,* Vol. **21,** pp. 219–229, eds Schäfer, T., Dohrmann, R. & Greenwell, H.C., The Clay Minerals Society.

Esefelder, R., Wawerzinek, B., Lüth, S., Giese, R. & Krawczyk, C.M., 2021. Seismic anisotropy of opalinus clay: tomographic investigations using the infrastructure of an underground rock laboratory (URL). *Swiss J. Geosci.,* **114**(1), doi:10.1186/s00015-021-00398-2.

Faoro, I., Vinciguerra, S., Marone, C., Elsworth, D. & Schubnel, A., 2013. Linking permeability to crack density evolution in thermally stressed rocks under cyclic loading: permeability and crack density evolution. *Geophys. Res. Lett.,* **40**(11), 2590–2595.

Faulkner, D.R., Jackson, C.A.L., Lunn, R.J., Schlische, R.W., Shipton, Z.K., Wibberley, C.A.J. & Withjack, M.O., 2010. A review of recent developments concerning the structure, mechanics and fluid flow properties of fault zones. *J. Struct. Geol.,* **32**(11), 1557–1575.

Faulkner, D.R., Mitchell, T.M., Jensen, E. & Cembrano, J., 2011. Scaling of fault damage zones with displacement and the implications for fault growth processes. *J. geophys. Res.,* **116**(B5), doi:10.1029/2010JB007788.

Faulkner, D.R., Mitchell, T.M., Rutter, E.H. & Cembrano, J., 2008. On the structure and mechanical properties of large strike-slip faults. *Geol. Soc., Lond., Spec. Publ.,* **299**(1), 139–150.

Geng, Z., Bonnelye, A., Chen, M., Jin, Y., Dick, P., David, C., Fang, X. & Schubnel, A., 2017. Elastic anisotropy reversal during brittle creep in shale: anisotropy reversal during creep. *Geophys. Res. Lett.,* **44**(21), 10 887–10 895.

Geng, Z., Bonnelye, A., Chen, M., Jin, Y., Dick, P., David, C., Fang, X. & Schubnel, A., 2018. Time and temperature dependent creep in Tournemire Shale. *J. geophys. Res.,* **123**(11), 9658–9675.

Gomila, R., Arancibia, G., Mitchell, T.M., Cembrano, J.M. & Faulkner, D.R., 2016. Palaeopermeability structure within fault-damage zones: a snap-shot from microfracture analyses in a strike-slip system. *J. Struct. Geol.,* **83**(February), 103–120.

Guglielmi, Y., Elsworth, D., Cappa, F., Henry, P., Gout, C., Dick, P. & Durand, J., 2015. In situ observations on the coupling between hydraulic diffusivity and displacements during fault reactivation in shales: permeability of an activated shale fault. *J. geophys. Res.,* **120**(11), 7729–7748.

Hedan, S., Cosenza, P., Valle, V., Dudoignon, P., Fauchille, A.-L. & Cabrera, J., 2012. Investigation of the damage induced by desiccation and heating of Tournemire Argillite using digital image correlation. *Int. J. Rock Mech. Min. Sci.,* **51**(April), 64–75.

Hirono, T., Kameda, J., Kanda, H., Tanikawa, W. & Ishikawa, T., 2014. Mineral assemblage anomalies in the slip zone of the 1999 Taiwan Chi-Chi Earthquake: ultrafine particles preserved only in the latest slip zone: mineral assemblage anomaly in slip zone. *Geophys. Res. Lett.,* **41**(9), 3052–3059.

Huang, Z., Tilmann, F., Comte, D. & Zhao, D., 2019. *P*-wave azimuthal anisotropic tomography in northern Chile: insight into deformation in the subduction zone. *J. geophys. Res.,* **124**(1), 742–765.

Hung, J.-.H., Ma, K.-.F., Wang, C.-.Y., Ito, H., Lin, W. & Yeh, E.-C., 2009. Subsurface structure, physical properties, fault-zone characteristics and stress state in scientific drill holes of Taiwan Chelungpu Fault Drilling Project. *Tectonophysics,* **466**(3–4), 307–321.

Ikari, M.J., Saffer, D.M. & Marone, C., 2007. Effect of hydration state on the frictional properties of Montmorillonite-Based Fault Gouge. *J. geophys. Res.,* **112**(B6), doi:10.1029/2006JB004748.

Jaeggi, D., Laurich, B., Nussbaum, C., Schuster, K. & Connolly, P., 2017. Tectonic structure of the 'Main Fault' in the Opalinus Clay, Mont Terri Rock Laboratory (Switzerland). *Swiss J. Geosci.,* **110**(1), 67–84.

Janssen, C., Kanitpanyacharoen, W., Wenk, H.-R., Wirth, R., Morales, L., Rybacki, E., Kienast, M. & Dresen, G., 2012. Clay fabrics in SAFOD core samples. *J. Struct. Geol.,* **43**(October), 118–127.

Jones, L.E.A. & Wang, H.F., 1981. Ultrasonic velocities in cretaceous shales from the Williston Basin. *Geophysics,* **46**(3), 288–297.

Josh, M., Esteban, L., Delle Piane, C., Sarout, J., Dewhurst, D.N. & Clennell, M.B., 2012. Laboratory characterisation of shale properties. *J. Pet. Sci. Eng.,* **88–89**(June), 107–124.

Laurich, B., Urai, J.L. & Nussbaum, C., 2017. Microstructures and deformation mechanisms in Opalinus Clay: insights from Scaly Clay from the Main Fault in the Mont Terri Rock Laboratory (CH). *Solid Earth,* **8**(1), 27–44.

Laurich, B., Urai, J.L., Desbois, G., Vollmer, C. & Nussbaum, C., 2014. Microstructural evolution of an incipient fault zone in Opalinus Clay: insights from an optical and electron microscopic study of ion-beam polished samples from the main fault in the Mt-Terri Underground Research Laboratory. *J. Struct. Geol.,* **67**(October), 107–128.

Lefèvre, M., Guglielmi, Y., Henry, P., Dick, P. & Gout, C., 2016. Calcite Veins as an Indicator of Fracture Dilatancy and Connectivity during Strike-Slip Faulting in Toarcian Shale (Tournemire Tunnel, Southern France). *J. Struct. Geol.* **83,** 73–84.

Masri, M., Sibai, M., Shao, J.F. & Mainguy, M., 2014. Experimental investigation of the effect of temperature on the mechanical behavior of Tournemire Shale. *Int. J. Rock Mech. Min. Sci.,* **70**(September), 185–191.

Matray, J.M., Savoye, S. & Cabrera, J., 2007. Desaturation and structure relationships around drifts excavated in the well-compacted Tournemire's Argillite (Aveyron, France). *Eng. Geol.,* **90**(1–2), 1–16.

Mitchell, T.M. & Faulkner, D.R., 2012. Towards quantifying the matrix permeability of fault damage zones in low porosity rocks. *Earth planet. Sci. Lett.,* **339–340**(July), 24–31.

Moreno, E. *et al.*, 2018. Fault imprint in clay units: magnetic fabric, p-wave velocity, structural and mineralogical signatures. *Tectonophysics,* **745,** 264–277.

Nhu, E.V., 2014. Détection des zones de failles par tomographie en transmission: application à la station expérimentale de Tournemire. 215.

Niandou, H., Shao, J.F., Henry, J.P. & Fourmaintraux, D., 1997. Laboratory investigation of the mechanical behaviour of Tournemire Shale. *Int. J. Rock Mech. Min. Sci.,* **34**(1), 3–16.

Orellana, L.F., Nussbaum, C., Grafulha, L., Henry, P. & Violay, M., 2022. Physical characterization of fault rocks within the Opalinus Clay formation. *Sci. Rep.,* **12**(1), doi:10.1038/s41598-022-08236-7.

Peacock, D.C.P., Dimmen, V., Rotevatn, A. & Sanderson, D.J., 2017. A Broader Classification of Damage Zones. *J. Struct. Geol.,* **102,** 179–192.

Rempe, M., Mitchell, T., Renner, J., Nippress, S., Ben-Zion, Y. & Rockwell, T., 2013. Damage and seismic velocity structure of pulverized rocks near the San Andreas Fault: damage structure of pulverized rocks. *J. geophys. Res.,* **118**(6), 2813–2831.

Rivet, D., De Barros, L., Guglielmi, Y., Cappa, F., Castilla, R. & Henry, P., 2016. Seismic velocity changes associated with aseismic deformations of a fault stimulated by fluid injection: seismic speed changes during fault slip. *Geophys. Res. Lett.,* **43**(18), 9563–9572.

Saffer, D.M. & Marone, C., 2003. Comparison of smectite- and illite-rich gouge frictional properties: application to the updip limit of the seismogenic zone along subduction megathrusts. *Earth planet. Sci. Lett.,* **215**(1–2), 219–235.

Savage, H.M. *et al.*, 2021. Asymmetric brittle deformation at the Pāpaku Fault, Hikurangi Subduction Margin, NZ, IODP Expedition 375. *Geochem. Geophys. Geosyst.,* **22**(8), e2021GC009662, doi:10.1029/2021GC009662.

Schubnel, A. & Guéguen, Y., 2003. Dispersion and anisotropy of elastic waves in cracked rocks: elastic waves in cracked rocks. *J. geophys. Res.,* **108**(B2), doi:10.1029/2002JB001824.

Schubnel, A., Benson, P.M., Thompson, B.D., Hazzard, J.F. & Young, R.P., 2006. Quantifying damage, saturation and anisotropy in cracked rocks by inverting elastic wave velocities. *Pure appl. Geophys.,* **163**(5–6), 947–973.

Séranne, M., 2014. Y a-t-il du gaz de schiste en Languedoc? *Ann. Soc. d'Hortic. d'Hist. Nat. l'Héranlt,* **154,** 80–95.

Solum, J.G., Hickman, S.H., Lockner, D.A., Moore, D.E., Pluijm, B.A., Schleicher, A.M. & Evans, J.P., 2006. Mineralogical characterization of protolith and fault rocks from the SAFOD main hole. *Geophys. Res. Lett.,* **33**(21), doi:10.1029/2006GL027285.

Thomsen, L., 1986. Weak elastic anisotropy. *Geophysics,* **51**(10), 1954–1966.

Torabi, A., Ellingsen, T.S.S., Johannessen, M.U., Alaei, B., Rotevatn, A. & Chiarella, D., 2020. Fault zone architecture and its scaling laws: where does the damage zone start and stop?. *Geol. Soc., Lond., Spec. Publ.,* **496**(1), 99–124.

Valès, F., Nguyen Minh, D., Gharbi, H. & Rejeb, A., 2004. Experimental study of the influence of the degree of saturation on physical and mechanical properties in Tournemire Shale (France). *Appl. Clay Sci.,* **26**(1–4), 197–207.

Vernik, L. & Nur, A., 1992. Ultrasonic velocity and anisotropy of hydrocarbon source rocks. *Geophysics,* **57**(5), 727–735.

Wang, H. *et al.*, 2020. Isotropic and anisotropic *P*-wave velocity structures of the crust and uppermost mantle beneath Turkey. *J. geophys. Res.,* **125**(12), doi:10.1029/2020JB019566.

Yamaguchi, A., *et al.*, 2011. Progressive illitization in fault gouge caused by seismic slip propagation along a megasplay fault in the Nankai trough. *Geology,* **39**(11), 995–998.

Zhang, H., 2003. Automatic P-wave arrival detection and picking with multiscale wavelet analysis for single-component recordings. *Bull. seism. Soc. Am.,* **93**(5), 1904–1912.